Everlasting Living and Breathing Gyroid 3D Network in Si@SiOx/C Nanoarchitecture for Lithium Ion Battery

Jaewoo Lee, Janghyuk Moon, Sang A Han, Junyoung Kim, Victor Malgras, Yoon-Uk Heo, Hansu Kim, Sang-Min Lee, Hua Kun Liu, Shi Xue Dou, et al.

ARTICLE

Everlasting Living and Breathing Gyroid 3D Network in Si@SiO_x/C Nanoarchitecture for Paving the Way to High Energy Lithium Storage Materials

Jaewoo Lee‡[a], Janghyuk Moon‡[b], Sang A Han[a,c], Junyoung Kim[d], Victor Malgras[e], Yoon-Uk Heo[f], Hansu Kim[g], Sang-Min Lee[h], Huakun Liu[a], Shi Xue Dou[a], Yusuke Yamauchi[i], Min-Sik Park*[d] and Jung Ho Kim*[a]

Silicon-based materials are the most promising candidates to surpass the capacity limitation of conventional graphite anode for lithium-ion batteries. Unfortunately, Si-based materials suffer from poor cycling performance and dimensional instability induced by the large volume changes during cycling. To resolve such problems, nanostructured silicon-based materials with delicately controlled microstructure and interfaces have been intensively investigated. Nevertheless, they still face problems related to their high synthetic cost and their limited electrochemical properties and thermal stability. To overcome these drawbacks, we demonstrate the strategic design and synthesis of a gyroid three-dimensional network in a Si@SiO_x/C nanoarchitecture (3D-Si@SiO_x/C) with synergetic interaction between the computational prediction and the synthetic optimization. This 3D-Si@SiO_x/C exhibits not only excellent electrochemical performance due to its structural stability and superior ion/electron transport, but also enhanced thermal stability due to the presence of carbon, which was formed by a cost-effective one-pot synthetic route. We believe that our rationally designed 3D-Si@SiO_x/C will lead to the development of anode materials for the next generation lithium-ion batteries.

Broader context

With the increasing global demand on the development of environmeltally friendly and renewable energy sources, lithium-ion batteries are emerging as one of the most promising energy storage applications. However, conventional graphite system as an anode is insufficient for satisfying the rapidly changing industrial needs due to its intrinsically low theoretical capacity and rate capability. Thus the development of new anode materials has become a prerequisite for taking a step forward the next generation LIBs. Herein, our new architecture based on silicon, which has drawn much attention as a promising anode material for various lithium storage systems, seems significantly novel and reasonably designed in terms of various functionalities such as mechanical robustness, thermal stability, and electrochemical performance in lithium-ion batteries. Moreover, with the synergetic interaction between computational prediction of the structure and synthetic optimization of the products, we figured out both suitable architecture and each individual role of components in the architecture. These results suggest that applicability and useful information can be derived for developing silicon-based anodes with high energy density.

[a] *Institute for Superconducting & Electronic Materials (ISEM), Australian Institute of Innovative Materials (AIIM), University of Wollongong, Innovation Campus, Squires Way, North Wollongong, NSW 2500, Australia, E-mail: jhk@uow.edu.au*
[b] *School of Energy Systems Engineering, Chung-Ang University, Seoul, Republic of Korea*
[c] *School of Advanced Materials Science & Engineering, Sungkyunkwan University (SKKU), Suwon, 440-746, Republic of Korea*
[d] *Department of Advanced Materials Engineering for Information and Electronics, Kyung Hee University, 1732 Deogyeong-daero, Giheung-gu, Yongin 17104, Republic of Korea, E-mail: mspark@khu.ac.kr*
[e] *International Center for Young Scientists (ICYS) & International Centre for Materials Nanoarchitectonics (MANA), National Institute for Materials Science (NIMS), 1-1 Namiki, Tsukuba, Ibaraki 305-0044, Japan*
[f] *Graduate Institute of Ferrous Technology (GIFT), Pohang University of Science and Technology (POSTECH), San 31, Hyoja-Dong, Pohang 790-784, Republic of Korea*
[g] *Department of Energy Engineering, Hanyang University, 222 Wangsimni-ro, Seongdong-gu, Seoul, 133–791, Republic of Korea*
[h] *Battery Research Center, Korea Electrotechnology Research Institute, 12 Bulmosan-ro, 10 beon-gil, Seongsan-gu, Changwon 51543, Republic of Korea*
[i] *School of Chemical Engineering and Australian Institute for Bioengineering and Nanotechnology (AIBN), The University of Queensland, Brisbane, QLD 4072, Australia*

† Electronic Supplementary Information (ESI) available.

‡ These authors contributed equally to this work.

Introduction

Silicon (Si) has been proposed as a promising anode material on account of its high theoretical specific capacity ($Li_{15}Si_4$, 3580 mA h g^{-1}) and relatively low redox potential versus Li/Li^+ (~0.4 V), as compared with the conventional graphite system, which shows intrinsically less theoretical capacity (372 mA h g^{-1})[1-5]. Severe volume expansion/contraction occurs, however, when the Si active materials are reacting with lithium (Li) in alloying/dealloying processes (> 300 %)[6]. The mechanical stress on the surface caused by the volume changes leads to the pulverization of the Si particles and the loss of electrical contact[7]. Consequently, it causes rapid capacity degradation during cycling. To overcome these drawbacks, recently, various approaches have been proposed, which are mainly divided into two research strategies. Firstly, to create morphological variations of Si active materials is mainstream research to reduce the mechanical stress such as with zero-dimensional

(0D) nanoparticles[8-10], one-dimensional (1D) nanorods/nanotubes[11-13], two-dimensional (2D) nanosheets[14,15], and three-dimensional (3D) porous materials[16-19], as well as microparticles[20,21]. These Si materials show not only excellent cycling performances, but also highly reversible specific capacities due to their enhanced anti-pulverization characteristics. It might be infeasible, however, to apply them in large-scale production because the material preparation requires high-cost synthetic routes or even the use of hazardous chemicals. Secondly, various types of Si-based composites have been introduced in order to compensate for the deficiencies of Si, such as Si/carbon composites[22-25], Si/SiO_x composites[26,27], and Si/alloy composites[28,29]. Although these composites also show moderate cycling performances, none of these materials is adequate enough to overcome the performance of conventional graphite, owing to different weaknesses, such as low initial Coulombic efficiency, high-cost synthesis, or high-cost precursors.

By considering previous research, it is argued that simultaneous troubleshooting on various aspects is a prerequisite for applying the Si-based anode materials in the next generation of Li-ion batteries (LIBs). To be specific, the Si-based anode materials should first have high reversible capacity with an acceptable initial Coulombic efficiency in order to surpass the energy density of the conventional graphite system. Unless these characteristics are sufficiently high, it might be nothing but a meaningless performance based on relatively low density structured materials such as nanosized or porous materials[30]. Secondly, they should have, needless to say, good cyclability assisted by structural modifications such as control of the particle size and the introduction of a robust framework for preventing the fracturing of the materials when they react with Li[5]. Thirdly, ion/electron conductivity and thermal stability are also essential factors that the Si-based anode materials should have. Regardless of the intrinsically insufficient properties of Si, these can be compensated by designing the suitable structures such as a 3D network, as well as the incorporation of carbon, which enhances the conductivity and the thermal stability[23,31]. Finally, the synthesis of the material should be conducted by using safe, nontoxic, and cost-effective methods for mass-scale production. Accordingly, these factors should be considered from the material design step. To sum up, we aim to achieve the development of Si-based materials for practical use under the consideration of 1) the high energy density (e.g. Si content), 2) robust structure with a combination of stable components (e.g. 3D network SiO_x), 3) high conductivity and thermal properties (e.g. carbon incorporation), and 4) facile synthesis.

On the basis of our strategies for material design, we engaged in computational predictions of the volume changes of various structures, as well as exploring how to realize the ideal material from the predictions with the aid of continuous feedback. By continuum scale analysis, simulation, and prediction of volume changes for both the unit cell and Si particles interior models were constructed to aid in the structural design of anode materials. We thus determined that our 3D network structured Si/SiO_x composite could prevent volume expansion as well as providing better ion/electron conductivity with Si-based anode. In this study, we consequently demonstrate a gyroid 3D network of Si embedded in SiO_x with a carbon shell as a new nanoarchitecture (denoted as 3D-Si@SiO_x/C) which was synthesized via one-step magnesiothermic reduction[32] and carbonization[33] with double-gyroid highly ordered mesoporous silica (denoted as KIT-6), including polymer template as a precursor. The 3D-Si@SiO_x/C has a mesoporous structure with 10 nm-sized, defect-rich Si nanoparticles interconnected in a SiO_x/C network frame. With this nanoarchitecture, the 3D-Si@SiO_x has delivered the reversible capacity of 1635 $mAhg^{-1}$, and its initial Coulombic efficiency is over 80% due to its structural stability. The 3D-Si@SiO_x has also demonstrated 83.3% stable capacity retention up to 100 cycles and 85.0% rate capability at a current density of 4000 mAg^{-1} compared to 200 mAg^{-1}. In addition, highly thermostable properties were confirmed by a high temperature cycling test at 60 °C and differential scanning calorimetry (DSC) analysis of the electrode after lithiation. As a result, we argue that rationally designed 3D-Si@SiO_x/C is the best candidate for the practical use of cost-effective and safe Si-based anode material for the next generation of LIBs.

Results and discussion

Prediction of volume changes and the consequent structural design

For finite element analysis, the 3D-Si@SiO_x/C structure with the Schoen's gyroid structure was modeled by level surfaces according to trigonometric functions as follows[34]:

$$\sin(x)\cos(y) + \sin(y)\cos(z) + \sin(z)\cos(x) = t \qquad (1)$$

where t is the constant of the level surface to control the volume fraction of gyroid networks which can be defined by the ratio of volume enclosed by the level surface to the other side. For the Si particle, the diameter of the sphere was defined by 10 nm, and the position of sphere was placed where the space was maximized in the gyroid structure. The threshold of the level surface was set to be $t = \pm 0.02$, which satisfies the condition that pore diameter of gyorid structure is 8 nm (Fig. S1, ESI†).

In order to analyze the volume expansion of Si particles in the prepared 3D structure, we have compared the changes in volume expansion of the Si particle in different structures. Fig. 1a shows the volume evolution of a free-standing Si particle up to 280 %. Fig. 1b shows the finite element analysis results for an embedded Si particle in a SiO_2 nanowire. During full lithiation, the Si core experiences compressive stress because the SiO_2 matrix prevents expansion outward. Due to the rigid matrix, there was a decrease in the volume change of about 30%. The thickness of nanowire matrix in the radial direction is thin, however, so the elastic supporting effects on Si were only applied in the direction of the height axis (z-axis) (for detailed information regarding lithiated SiO_2 effects, see Fig. S2 with explanations, ESI†). In the gyroid SiO_2 matrix, the Si particle shows lower volume expansion from 200 % to 230% depending

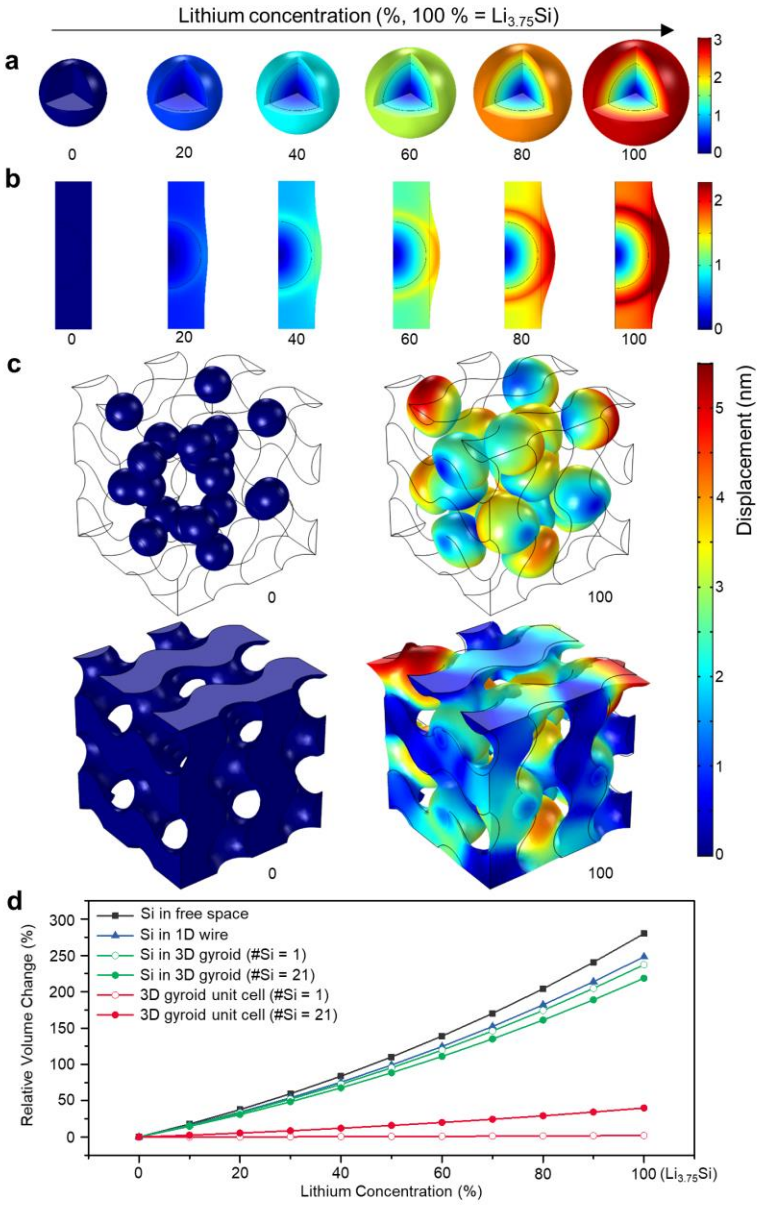

Fig. 1 Continuum scale analysis for the simulation of particle and unit volume changes in silicon-based materials before and after full lithiation. (a) Si nanoparticle in free space. (b) Si nanoparticle embedded in 1D-SiO_2 structure. (c) Si nanoparticles embedded in a 3D network gyroid structure and the total unit of the gyroid 3D network Si@SiO_x. (d) Comparison of the relative volume changes of (a-d) during lithiation. #Si indicates the number of Si nanoparticles randomly located inside the gyroid structure from #Si = 1 to #Si = 21 (fully packed).

on the number of Si particles or the volume ratio of Si compared to the gyroid matrix, as shown in Fig. 1c and 1d. The perfect gyroid lattice has cubic symmetry, and the embedded Si particle deforms under macroscopic hydrostatic pressure. Compared to the 1D nanowire, the effective suppression of lithium compositional expansion is attributed to the axisymmetric 3D network geometry. Furthermore, the unit cell of the gyroid structure provides free space to accommodate the volume changes of the embedded Si particles. The overall volume expansion ratio is greatly reduced by up to 50%. (Movie Clips of each structures shown in Fig. 1a, 1b, and 1c during lithiation are can be found in the additional electronic supplementary files. The color maps of each structure according to the volume changes are shown in Fig. S3, ESI†.)

Synthesis of the 3D-Si@SiO_x/C

Fig. 2a shows a schematic illustration of the strategically designed 3D-Si@SiO_x/C synthetic process from double-gyroid KIT-6, including the polymer template. According to the results of the simulation of the volume changes, we adopted the KIT-6 that is interlaced with two gyroidal forms of silica and polymer as a precursor[35]. We expect that the KIT-6 will give a 3D network structure with appropriate contents of silicon, and it is also suitable for controlling the formation of the pores and Si

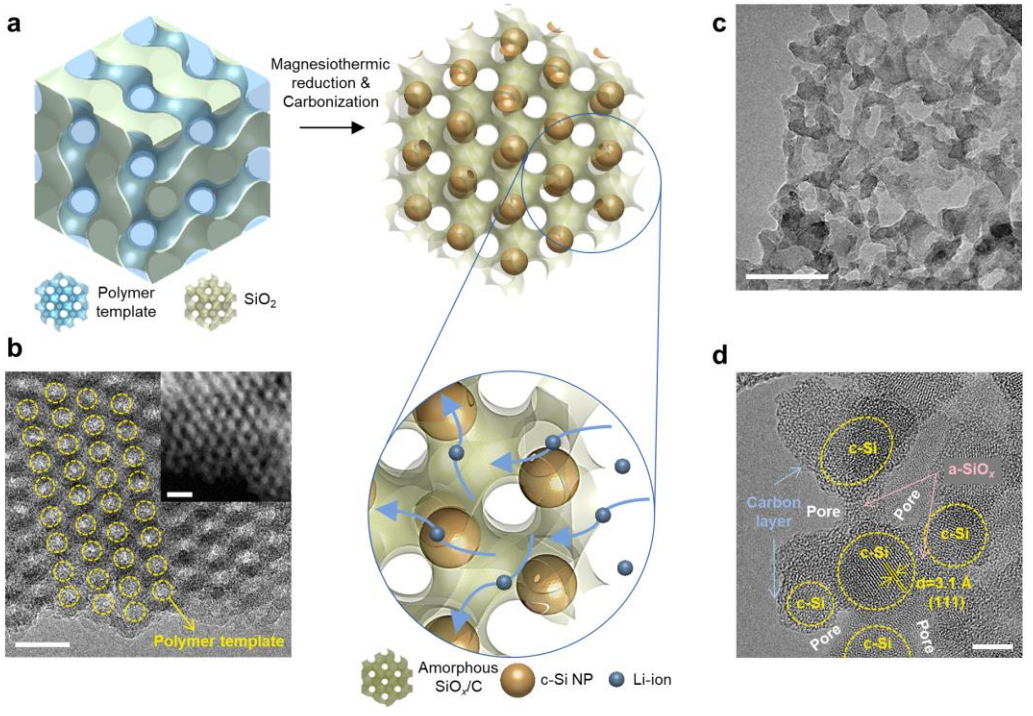

Fig. 2 Synthesis of gyroid 3D network of Si@SiO_x/C. (a) Schematic illustration of the synthetic route for the 3D-Si@SiO_x/C via one-pot magnesiothermic reduction and carbonization of the KIT-6, including the polymer template. (b) Transmission electron microscope (TEM) image of highly ordered double-gyroid KIT-6 including polymer template with its high angle annular dark field – scanning TEM (HAADF-STEM) image in the inset. (c-d) TEM image of the 3D-Si@SiO_x/C (c) and its corresponding HRTEM image (d), showing that the c-Si particles are interconnected inside the SiO_x/C network frame. Scale bars, 20 nm for (b, including inset) and (c), 5 nm for (d).

materials. Moreover, the polymer template could be partly converted to carbonized form which will play a role in the enhancement of the electrical conductivity and the mechanical strength of the material[27,33]. Owing to our series of the logical ways to seek an optimum material, the obtained material is expected to provide exceptional value in battery performance.

To meet the requirements above, the KIT-6, including the polymer template mixed with magnesium (Mg) as reducing agent, is sealed in a stainless steel reactor and activated at 750 °C for 2 h in argon. Subsequently, the resulting product is washed with hydrochloric acid (HCl) to remove residual Mg compounds. Finally crystalline Si nanoparticles (c-Sis) embedded in a SiO_x/C network are obtained. That is to say, well-aligned gyroid SiO_x with carbon shell as well as embedded c-Sis cores is derived from highly ordered double-gyroid KIT-6, including the polymer template (Fig. 2b and Fig. S4, ESI†). Although the morphology of the obtained material appeared slightly distorted compared to its precursor (Fig. 2c), the gyroid 3D network structure was still maintained, and it also possessed mesopores where the polymer template was located. Moreover, the polymer templates were transformed into carbon shells. The c-Si particles were interconnected inside the SiO_x/C network frame (Fig. 2d). Detailed high resolution transmission electron microscope (HRTEM) image confirms the presence of c-Si with a lattice spacing of 0.31 nm, corresponding to the (111) planes of the face-centered cubic structure[36,37,27].

Material optimization and characterizations of the 3D-Si@SiO_x/C

According to the predictions of the model, our desirable material should maintain its 3D network mesoporous structure with a large fraction of c-Si particles and SiO_x/C (or SiO_x) as a shell-like frame. To meet the above requirements, two kinds of synthesis were conducted. Firstly, heat-treatment temperatures were fixed at 675, 750, and 825 °C (with the samples denoted as 675, 750, and 825, respectively) for yielding an optimum ratio of c-Si particles while inducing partial reduction of silica. Secondly, calcined KIT-6 (which contains only silica) and uncalcined KIT-6 (which includes polymer template) were used as precursors (denoted as w/o and w/ polymer template, respectively) for determining the effects of the carbon which was acquired from the carbonization of the polymer template[38]. For comparative study, characterizations and electrochemical measurements of commercial Si nanopowder (denoted as Si-NP, 50 nm, Sigma Aldrich) were also conducted concurrently.

Fig 3a shows the X-ray diffraction (XRD) patterns of the reference Si-NP and the as-prepared six samples after HCl washing. Diffraction peaks of face-centered cubic silicon are clearly shown at 28.6, 47.6, 56.5, 69.7, and 77.0°, whereas c-Si and other magnesium compounds (MgO, Mg_2Si, and Mg_2SiO_4) co-existed in all six samples before HCl washing (Fig. S5a, ESI†)[39]. The content of c-Si also increased with increasing reaction temperature. Interestingly, there was unwanted Mg_2SiO_4, which could not be removed in HCl solution in the case

of the 825 samples (825s)[40,41]. Through detailed transmission electron microscopy (TEM) of the six products, predominant morphological differences were observed as a function of the heat-treatment temperature. While 675s and 750s maintained their original mesoporous structures, the pores were collapsed and the particles were agglomerated to form larger lumps in the 825s (Fig. S5b, ESI†). On increasing the temperature from 675 °C to 825 °C, the average crystalline silicon size had a tendency to increase from ~4 nm in the 675s and ~8 nm in the 750s to ~17 nm in the 825s, respectively (Fig. 3b). Due to these morphological differences and the content/size diversity of the c-Si particles, it could be expected that distinguishing electrochemical outputs would be shown. Fig. 3c, 3d, and 3e show the electrochemical properties of the six products and Si-NP. The specific discharge capacities (at the first cycle) of the 825s are the highest, as expected (2294 and 2349 mAh g^{-1} for the w/o and w/ polymer template, respectively), whereas the 675s showed insignificant specific capacities due to insufficient reduction of silica. On the other hand, compared to the other products and also the Si-NP reference, the 750s showed better initial Coulombic efficiencies of up to 80.1 %. In particular, outstanding cycling performance was shown in the 750-w/

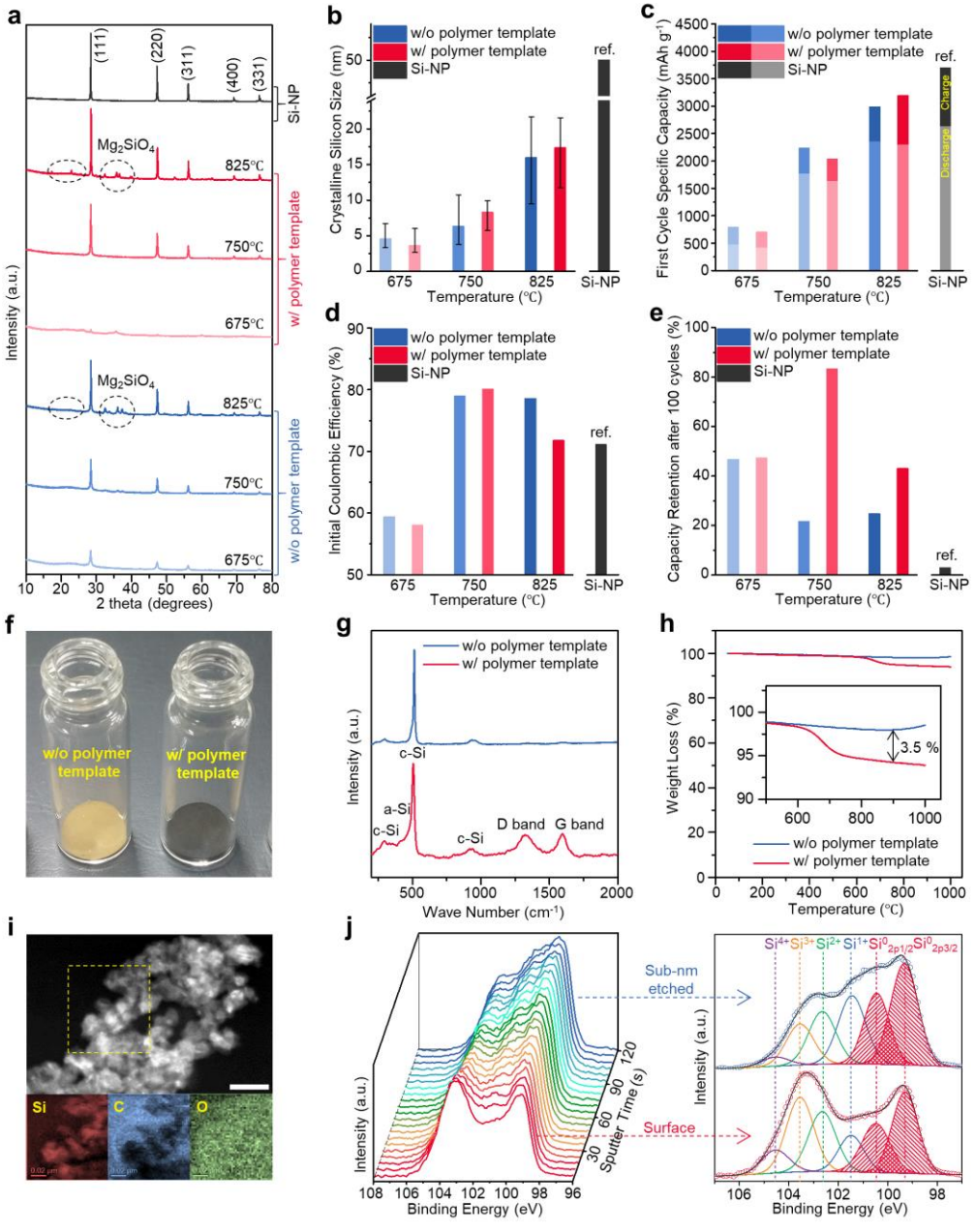

Fig. 3 Structural and electrochemical characterizations of various types of products. (a) XRD patterns of 6 products and reference Si NP. (b-e) Physical and electrochemical properties of 6 products and reference Si NP: c-Si particle sizes (b), specific capacities (c), initial Coulombic efficiencies (d), and cyclability (e). (f-h) confirmation of the presence of carbon: powder images (f), Raman spectra (g) and thermogravimetric analysis (TGA) curves (h) of 750-w/o and w/ polymer template samples. (i) Electron energy loss spectroscopy (EELS) elemental mapping images of the 750-w/ polymer template. (j) XPS Si 2p spectra of the 750-w/ polymer template during Ar^+ sputtering for 120 seconds. Scale bar, 50 nm for (i).

polymer template sample (over 80 % capacity retention after 100 cycles) in spite of the poor cyclability of all the other samples (under 50 %). (Detailed information, including numerical figures, is introduced in Fig. S6, ESI†.)

In order to investigate the distinction between the w/o and w/ polymer template samples, we conducted additional analyses on 750s. At first, from the color of the samples (w/o polymer template: light brown, w/ polymer template: black, as shown in Fig. 3f), the presence of carbon on the w/ polymer template can be detected. Fig. 3g shows Raman spectra of samples w/o and w/ polymer templates. Each exhibited three distinct peaks at 506, 299, and 940 cm^{-1}, which indicated crystalline silicon with its long-range order[42,43]. In the w/ polymer template sample, there was a broad peak near 450 cm^{-1}, which indicated amorphous silicon containing amorphous oxides due to its SiO_x framework whereas this barely appeared on the w/o polymer template sample. In particular, 2 broad peaks at 1331 and 1595 cm^{-1} corresponded to the D band and G band of carbon[44]. By thermogravimetric analysis, the content of carbon in the w/ polymer template sample was estimated to be 3.5 wt % (Fig. 3h). Also, it was confirmed that amorphous carbon covered all of the material, as determined from the electron energy loss spectroscopy (EELS) mapping images (Fig. 3i). These results indicated that 3.5 wt % of amorphous carbon was derived from the polymer template, which played a significant role between the c-Si particles and the SiO_x framework, enhancing the electrochemical reversibility and cyclability.

To confirm in-depth the mechanical and chemical properties of 750-w/ polymer template (target product), further characterizations were performed by using the Brunauer-Emmett-Teller (BET) technique, and XRD and X-ray photoelectron spectroscopy (XPS) measurements. The N_2 adsorption/desorption isotherm and pore size distribution results shown in Fig. S7 (ESI†) indicate that 750-w/ polymer template still maintained the surface area of 161 $m^2\ g^{-1}$ and its average pore size of 8.7 nm after one-step reduction/carbonization and further HCl washing, even if the amorphous precursor underwent crystallization of silicon, as identified from XRD results (Fig. S8, ESI†). Moreover, we confirmed that the metallic silicon is embedded inside nonstoichiometric silicon oxides by changes in the XPS Si 2p signals, which were continuously measured 21 times for 120 seconds during Ar^+ sputtering (Fig. 3j). From the surface to a sub-nm depth of the material, metallic Si^0 peaks at about 99.2 and 100.1 eV showed a gradual increase, while other silicon oxides peaks, which can be divided into Si^{1+}, Si^{2+}, Si^{3+} and Si^{4+} ($SiO_{0.5}$, $SiO_{1.0}$, $SiO_{1.5}$, and SiO_2, respectively) in the range from 101.4 to 104.6 eV, showed an obvious decrease[45]. Also, a slight increase and decrease in the atomic concentrations of elemental Si and O, respectively, were confirmed by the calculations based on the XPS survey scans (Fig. S9a and S9b, ESI†). In addition, the C 1s and O 1s signals indicate that carbon exists in an independent amorphous carbon form, while the oxygen in the material is mainly from silicon oxides (Fig. S9c and S9d, ESI†)[46]. Overall, it is demonstrated that 750-w/ polymer template has 10 nm crystalline silicon particles embedded in nonstoichiometric silicon oxides with an amorphous carbon layer forming a 3D network (Note that the name of the target product, which has been called 750-w/ polymer template so far will be changed again to 3D-Si@SiO_x/C hereafter.)

Effect of defects in silicon nanoparticles

Meanwhile, the 3D-Si@SiO_x/C possesses abundant defects inside most of the Si nanoparticles. As shown in Fig. 4a, defects such as twins and stacking faults, are extended from one side to the other side, passing through the bulk of Si nanoparticles. Moreover, each defect is randomly located on different positions. This might be because the 3D-Si@SiO_x/C was synthesized by the method of partial reduction of silica at relatively low temperature, which caused imperfect formation of the c-Si particles[47]. It is well known that defects in the crystal structure enhance ionic conductivity because they provides more free volume to accommodate the interstitial Li atoms than a perfect lattice[48]. In addition, according to a recent report, a defect-abundant Si anode shows better electrochemical performance in LIBs[49]. In order to investigate in depth how the defects affect the electrochemical properties of the 3D-Si@SiO_x/C anode, two different types of lithiation behavior depending on the existence of defects in the Si nanoparticles were also investigated. To obtain clear lithiated samples with no interference from a binder or a conductive agent, chemical lithiation by direct contact between the 3D-Si@SiO_x/C powder and Li-metal foil in the electrolyte for 6 hours was induced, as shown in Fig. 4b. In the TEM observation shown in Fig. 4c, the Si nanoparticle without defects exhibited a typical behavior in which amorphous lithium silicide (a-Li_xSi) enclosed c-Si (lattice spacing of 3.1 Å corresponding to the (111) planes) from the surface to deep inside of the bulk. On the other hand, interestingly, the Si nanoparticle which had a twin boundary formed crystalline lithium silicide (c-$Li_{15}Si_4$, lattice spacing of 6.1 Å, corresponding to the (111) planes) around the twin boundary. Morover, the c-$Li_{15}Si_4$ began to form even from inside of the bulk, not from the surface. This contrasting result clearly indicates that defects provide not only enhanced Li-ion diffusivity, which facilitates easy Li-ion transport to the bulk, but also a stable configuration in fully lithiated form without significantly affecting the mechanical strength in the case of the first cycle lithiation. Consequently, this result reflects the reason why the 3D-Si@SiO_x/C exhibits outstanding initial Coulombic efficiency with no drastic capacity degradation in the first several cycles, in contrast with conventional Si-based anode[50,27]. (Detailed outcomes regarding the electrochemical performance of the 3D-Si@SiO_x/C will be discussed next.)

To demonstrate Li kinetics in defects of c-Si structure, we conducted a density functional theory (DFT) simulation of Li migration in both defect-free c-Si and a particle with a twin grain boundary. We first examined Li migration in a c-Si structure composed of 64 Si atoms (2 × 2 × 2 supercell). An interstitial Li atom was positioned at a tetrahedral (Td) site (Fig. 4d). The diffusion pathways and activation energy barriers were carried out using the nudged elastic band (NEB) method. As shown in Fig. 4e, the Li migration is allowed along the pathway from one Td to another Td site through a hexagonal (Hex) ring where the

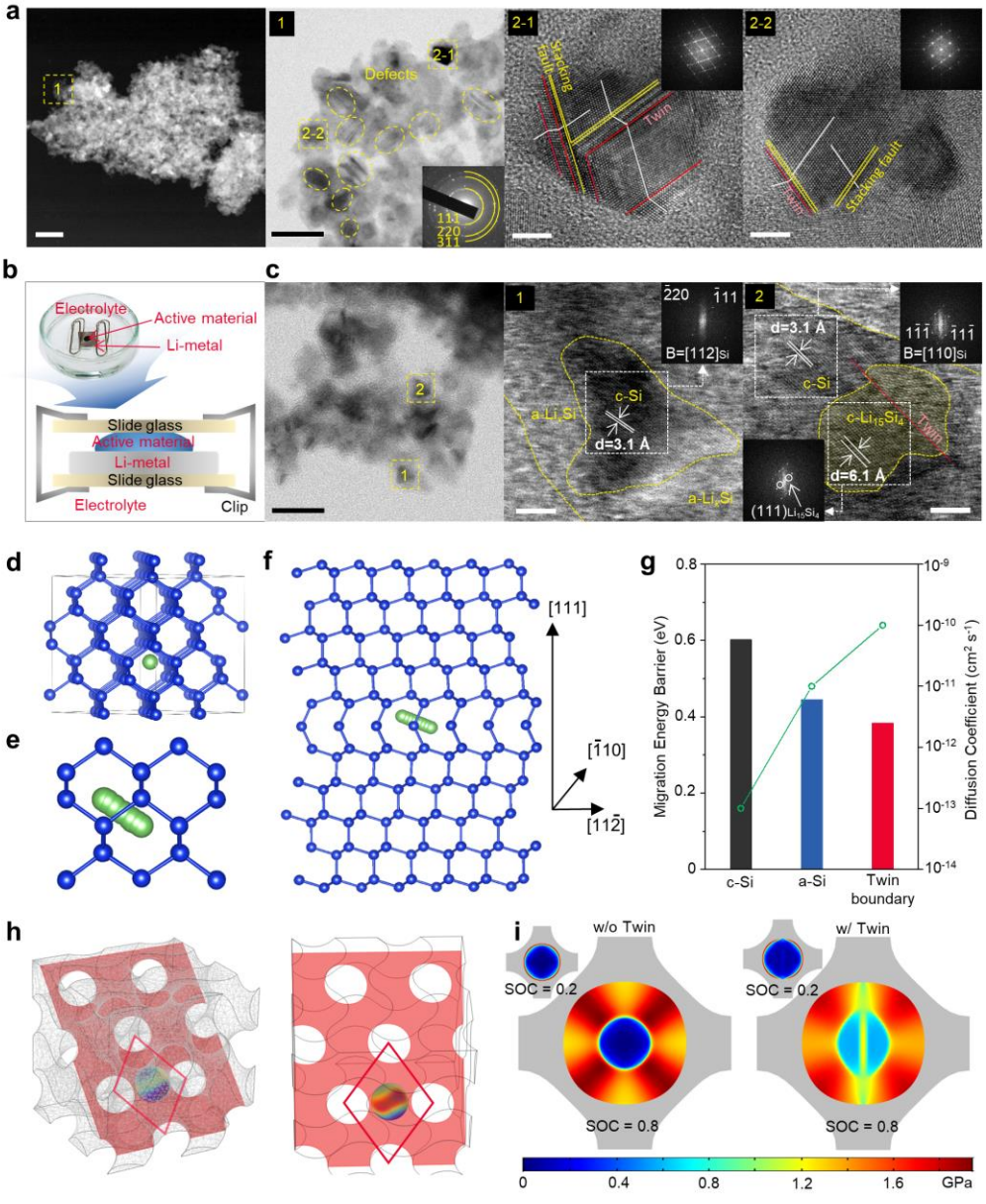

Fig. 4 Effect of defects in Si NPs. (a) TEM observations of abundant defects in Si NPs of the 3D-Si@SiO$_x$/C, with SAED patterns in the insets. (b) Photograph with description of the method for inducing chemical lithiation on the 3D-Si@SiO$_x$/C. (c) TEM observations of different types of lithiation behavior, depending on the existence of defects in the Si NPs. Scale bars, 100 nm, 50 nm, 5 nm, 5 nm for (a), 50 nm, 5 nm, 5 nm for (b). (d) Li interstitial atom in tetrahedral pore of Si supercell. (e) Li atom transition to the neighbouring tetrahedral sites. (f) Atomistic configuration of twin boundary and representative Li migration. (g) Migration energy barriers calculated by the climbing-image nudged elastic band (NEB) method and corresponding diffusion coefficient in c-Si, amorphous (a)-Si, and through the twin boundary. (h) Geometry of 3D gyroid structure with Si nanoparticle and 2D projected representative volume element for the Si@SiO$_x$/C network structure. (i) Stress evolution of Si particle in SiO$_x$ matrix during lithiation without and with a twin defect. (SOC: state of charge)

migration energy barrier was calculated to be 0.602 eV in the [111] direction.[51] As shown in Fig. 4f, the twin defect was generated using a supercell oriented along the usual axis for defect modeling, $\hat{x} = [11\bar{2}], \hat{y} = [\bar{1}10], \hat{z} = [111]$. The mirror plane is normal to $\hat{y}$ and placed in the middle of the surface. To reduce effects from the periodic boundary condition, we introduced void space more than 3.7 Å in thickness into the supercell in the z-direction. The stable Li interstitial sites were determined by the Delaunay triangulation method to find the large void sites. The Li interstitial diffuses along the spacious octagon ring, where the corresponding migration barrier is 0.384 eV. The Li interstitial is easier to diffuse along the twin boundary and harder to diffuse out along the Td→Hex→Td pathway in the c-Si lattice. Furthermore, the energy barrier of Li hopping in the twin boundary is lower than that in the amorphous structures, and the diffusion coefficient is also higher (Fig 4g)[52]. This indicates that the twin boundary provides enhanced Li-ion diffusivity. Fig. S10 (ESI†) shows representative

results for the Li concentration distribution in the case of Si nanoparticle with and without a twin defect. Sharp phase evolution is observed during first lithiation in c-Si[53]. The enhanced diffusivity in the twin defect changes the Li distribution for c-Si. The radial Li concentration, as shown in Fig. S10c (ESI†), shows that both center and surface regions are quickly lithiated in the case with the twin defect, while the Li barely exists in the central region of the particle without the twin defect, as shown in Fig. S10d (ESI†).

To explain the mechanical stability in detail, we present the stress variation in a representative volume element of the 3D gyroid structure, and a 2D projected gyroid structure with a Si particle is used for reducing the computational cost (Fig. 4h). In the initial lithiation, the newly generated Li-Si interphase expands more toward the surface direction rather than the core direction. The Si core experiences hydrostatic pressure (compressive stress) because the SiO_x matrix prevents outward expansion. Although the interconnected network frame of the SiO_x matrix well supports the Si nanoparticle, the relatively thin matrix in the void generates large von Mises stress, which results in mechanical failure. On the other hand, with the twin defect, the enhanced diffusion of Li makes the Li concentration distribution more even. The asymmetric von Mises stress is also generated, but the magnitude of values for the von Mises stress is reduced (Fig 4i and Fig. S11, ESI†). We can argue that more evenly distributed lithiation ensures mechanical stability and that the defects in the Si nanoparticles of the 3D-Si@SiO_x/C significantly affect the mechanical strength at the first cycle.

Electrochemical performances and *ex-situ* TEM and SEM observations

The electrochemical properties of the 3D-Si@SiO_x/C and the commercially available Si-NP as a reference were estimated to validate the feasibility of the 3D-Si@SiO_x/C as an anode material. Fig. 5a shows galvanostatic charge-discharge curves of the first cycle at a current density of 200 mA g^{-1} in the voltage window of 0.01 V to 2.00 V (*vs.* Li/Li^+). The 3D-Si@SiO_x/C anode presented the same reduction/oxidation behavior as the Si-NP anode at a typical redox potential of 0.4 V during discharge[5], even though it was a mixed composite of c-Si, SiO_x, and C. This is because c-Si plays a major role in the specific capacity of the anode. It should be noted that the 3D-Si@SiO_x/C anode showed specific charge and discharge capacities of 2043 and 1635 mAh g^{-1}, respectively. In contrast, the Si-NP anode exhibited almost doubled specific capacities (3704 and 2631 mAh g^{-1}, respectively). Nevertheless, in terms of an anode performance, the 3D-Si@SiO_x/C anode showed not only a large enough reversible capacity of 1635 mAg g^{-1}, but also an outstanding value for the initial Coulombic efficiency (80.1 %). In addition, 83.3 % discharge capacity retention was observed even after 100 cycles, maintaining over 99.8 % Coulombic efficiency (Fig. 5b and inset). Thus, it seems that the 3D-Si@SiO_x/C anode would give a high energy density even at a reasonable electrode loading mass of 3.0 mg cm^{-1}. Moreover, the rate-capability was also characterized, as shown in Fig 5c and 5d. Compared to the discharge capacity of the 3D-Si@SiO_x/C anode at the current density of 200 mA g^{-1}, 85 % of the discharge capacity (1342 mAh g^{-1}) was still retained when a current density of 4000 mA g^{-1} was applied. Also, the capacity returned back stably to its original specific capacity at the current density of 200 mA g^{-1}, even after undergoing a high current density of 4000 mA g^{-1}.

In order to understand the structural stability of both the electrode and the particles inside of the 3D-Si@SiO_x/C anode during cycling, detailed microscopic observations were carried out by using *ex-situ* field emission SEM (FESEM) and TEM observations. Fig. 5e, 5f, 5g, and 5h show cross-sectional FESEM images of the 3D-Si@SiO_x/C electrode at different states of charge. The thickness of the pristine electrode was 26.9 µm after compression of the electrode. After full lithiation, the electrode volume expanded by only 9.3 % from its initial status. In principle, this result is well consistent with our computational simulation results on the volume expansion of the gyroid 3D network with Si@SiO_2. Moreover, the electrode still maintained its volume, even at 100 cycles, after undergoing a slight shrinkage due to the delithiation. It is expected that the stable cyclability was caused by its mechanical stability. Other *ex-situ* observations for determining the structural stability of the 3D-Si@SiO_x particles during cycling were conducted, as shown in Fig. 5i, 5j, 5k, and 5l. In these TEM observations, we confirmed that the expanded Li_xSi particles occupied the spaces where the voids originally were, and the Si particles returned back to their original positions while maintaining the mesoporous structure due to the robust SiO_x/C framework. Even after 100 cycles, the structure mainly remained the same, although partially collapsed and agglomerated particles can be observed (Fig. S12). Therefore, in sum, the 3D-Si@SiO_x/C surely has the potential for high electrochemical performance, even after long-term cycling, due to its outstanding high capacity in coordination with its structural stability.

Thermostability Properties

In order to confirm the thermal stability of the 3D-Si@SiO_x/C anode, we first examined its high-temperature cyclability, which gives a direct reflection of its thermostability characteristics. Fig. 6a shows first cycle charge-discharge profiles at different temperatures: room temperature (23 °C, RT) and 60 °C. It is generally understood that slightly increased reversible capacity (1746 mAh g^{-1}) and relatively low over potential were shown at 60 °C compared to at RT (1635 mAh g^{-1}) due to the increase in thermodynamic activity and ionic mobility at high temperature[54]. Above all, the 3D-Si@SiO_x/C anode showed good high temperature cyclability with capacity retention of 79.4 % over 70 cycles as well as maintaining high oulombic efficiency of 99.6 % (Fig. 6b). To investigate the thermal stability with temperature, which is closely related to the thermal reliability of full-cell configurations, DSC measurements of fully lithiated anodes were performed. Fig 6c shows the DSC curves of the 3D-Si@SiO_x, 3D-Si@SiO_x/C, and Si-NP electrodes in the state of full lithiation together with electrolyte inside each cells. The Si-NP electrode underwent severe exothermic reactions at the temperatures of 270 and 310 °C due to structural collapse followed by continuous

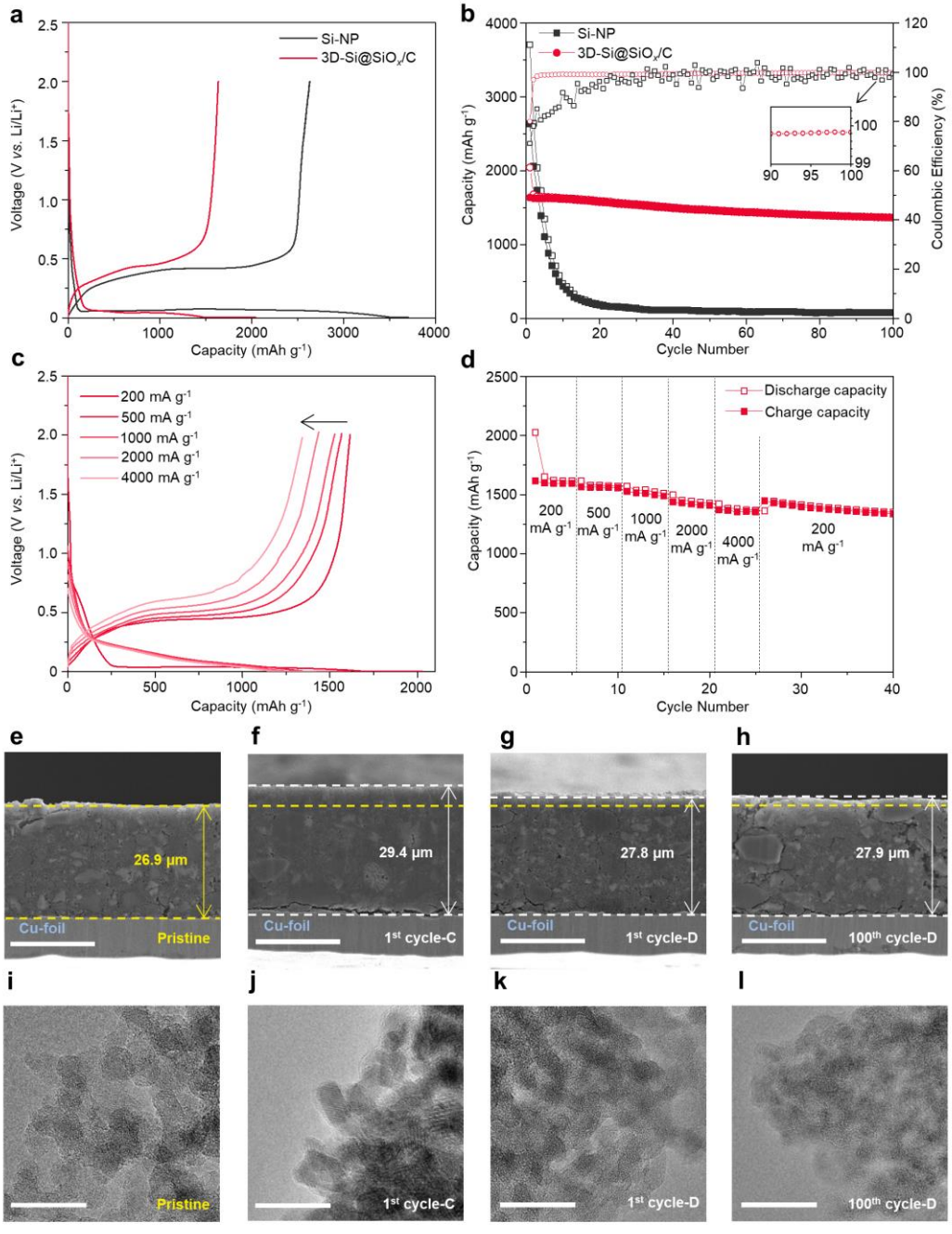

Fig. 5 Electrochemical performances and ex-situ TEM and SEM observations. (a) Galvanostatic charge-discharge profiles of the 3D-Si@SiO_x/C and Si NP anodes. (b) Cycling performances (closed symbol: discharge capacity, open symbol: charge capacity) and Coulombic efficiencies of the 3D-Si@SiO_x/C and Si NP anodes at a current density of 200 mA g^{-1}. (c-d) Galvanostatic charge-discharge profiles (c) and cycling performance (d) of the 3D-Si@SiO_x/C at different output current densities of 200, 500, 1000, 2000, and 4000 mA g^{-1}. (e-h) Cross-sectional SEM images of the 3D-Si@SiO_x/C electrodes at different cycles: pristine (e), first cycle charged (1st cycle-C) (f), first cycle discharged (1st cycle-D) (g), and hundredth cycle discharged (100th cycle-D) (h). (i-l) HRTEM observations of the Si-NP particles at different reaction states; pristine (i), 1st cycle-C (j), 1st cycle-D (k), and 100th cycle-D (l). Scale bars, 20 μm for (e-h), 20 nm for (i-l).

decomposition of lithium silicide phases and the electrolyte[55]. On the other hands, the 3D-Si@SiO_x/C showed gentle exothermic peaks due to its enhanced thermal stability by incorporation of carbon, while the 3D-Si@SiO_x also showed relatively sharp peaks in the temperature range from 200 °C to 350 °C. In addition, the accumulated heat generation calculated from the DSC curves was also investigated, as shown in fig. 6d. From room temperature up to 400 °C, the exothermic enthalpy, that is to say, the overall heat generation of the 3D-Si@SiO_x/C, the 3D-Si@SiO_x, and Si-NP electrodes is 10.0, 14.5, and 21.2 kJ g^{-1}, respectively. This result indicates that the 3D-Si@SiO_x/C exhibits improved thermal stability compared to the Si-NP and even the 3D-Si@SiO_x[56]. We strongly argue that thermal reliability is a necessary condition that anode materials must satisfy and that the importance of thermal stability cannot be emphasized enough. Consequently, our material can be

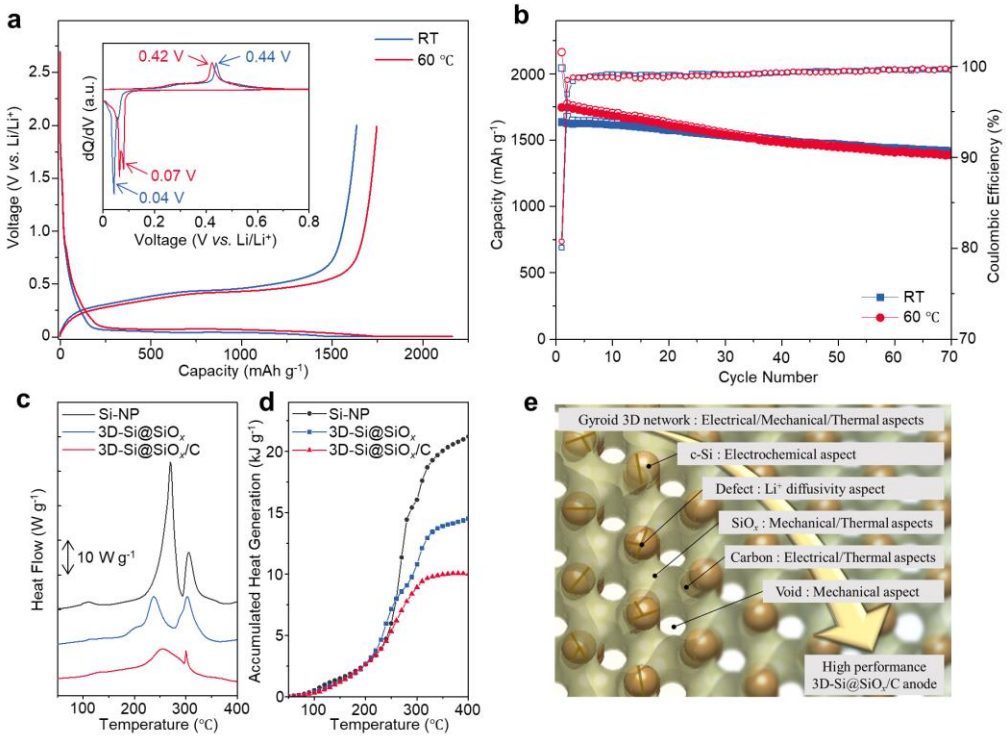

Fig. 6 Thermostability properties. (a) First cycle charge-discharge profiles, corresponding differential capacity plots (inset).(b) Cycling performances of 3D-Si@SiO_x/C at RT and 60 °C. (c-d) DSC curves (c) and corresponding cumulative heat generation profiles (d) of the 3D-Si@SiO_x/C, Si@SiO_x, and Si NP electrodes after full lithiation[56]. (e) Various aspects of the individual contents of the 3D-Si@SiO_x/C.

effective for preventing a sudden explosion of the battery under harsh conditions such as exposure to high temperature or mechanical compression/ distortion/ stabbing of the battery.

Overall, In order to obtain a high performance Si-based material, each component in the anode material should systematically play its role in various aspects, as shown in Fig. 6e. In detail, (I) the gyroid 3D network nanoarchitecture in electrical, mechanical, and thermal aspects, (II) the c-Si in the electrochemical aspect, (III) the defects in c-Si in the Li^+ diffusivity aspect, (IV) the SiO_x in mechanical and thermal aspects, (V) the carbon in electrical and thermal aspects, and finally (VI) the void space in the mechanical aspect; all should be combined for the final goal of the Si-anode material.

Conclusions

In this study, in order to optimize the material to obtain better electrochemical performance, both computational prediction of the structure and synthetic optimization of the products were considered. With the synergetic interaction between the two separate methods, we identified that the Si-based anode should have a robust and well-aligned 3D network structure with nanopores to prevent the volume expansion which affects electrode-level dilatation, as well as having suitable Si, SiO_x, and C contents in order to perform their own roles. Moreover, by controlling the synthetic conditions, the optimum materials could be obtained, and the computational predictions could also be proved.

From the point of view of Si-based anode materials, this 3D-Si@SiO_x/C exhibits three unique features. (I) The 3D network and mesoporous structure prevents volume expansion and promotes ion/electron transport when it reacts with Li[57,58]. Consequently, it provides excellent electrochemical performance. (II) Incorporation of carbon enhances the thermal stability of the electrode, which was determined from the reduced heat flow and moderate exothermic reaction in the DSC results, and hence, the 3D-Si@SiO_x/C showed stable high temperature cyclability. (III) One-step magnesiothermic reduction and carbonization synthesis without the use of hydrofluoric acid indicates the feasibility of mass production due to its cost-effectiveness and safety. We believe that this innovative 3D-Si@SiO_x/C nanoarchitecture will lead to the development of anode materials for the next generation of LIBs.

Methods

Numerical simulation modeling

Finite element analysis of the mechanical models was carried out using COMSOL Multiphysics. For diffusion-induced stress analysis of Li_xSi as function of Li concentration, Young's modulus from 90 to 40 GPa and Poisson's ratio from 0.28 to 0.24 was adopted[59]. Although the Li_xSiO_2 also shows elastic softening due

to Li insertion, we assumed that silica rarely reacts with lithium in this study.

The increment of elastic strain, $d\varepsilon_{ij}^{e}$, represents the Hooke's law:

$$d\varepsilon_{ij}^{e} = \frac{1}{E(c)}\left[\left(1+v(c)\right)d\sigma_{ij} - v(c)d\sigma_{kk}\delta_{ij}\right] \quad (2)$$

where $E(c)$ and $v(c)$ are the Young's modulus and Poisson's ratio as function of Li concentration, respectively. σ_{kk} is the diagonal components of stress and δ_{ij} is the Kronecker delta.

The classical J2-flow plasticity theory is employed to determine the increment of the plasticity strain, $d\varepsilon_{ij}^{p}$, refered to as:

$$d\varepsilon_{ij}^{p} = \dot{\lambda}\sigma_{ij}' \quad (3)$$

where $\dot{\lambda}$ is a scalar coefficient calculated by solving the boundary value problem. The yield strength of pristine Si is set at 1.75 GPa. Due to the lack of reported values of for the yield strength of Li_xSiO_2, we found the yield point of 20 GPa for $Li_{0.125}SiO_2$. (Detailed calculation results including the calculation method are introduced in Fig. S2, ESI†.)

Analogously, the increment of the compositional strain obeys following equation (4):

$$d\varepsilon_{ij}^{c} = \frac{\Omega dc}{3}\delta_{ij} \quad (4)$$

where Ω is the partial molar volume of the solute. As lithium is inserted into the silicon, the mechanical deformation arising from lithiation is divided into the reversible elasticity, irreversible plasticity, and compositional swelling contribution. The total incremental strain is the sum of each component as expressed in the equation (5):

$$d\varepsilon = d\varepsilon_{ij}^{e} + d\varepsilon_{ij}^{p} + d\varepsilon_{ij}^{c} \quad (5)$$

A diffusion model containing two-phase interfaces is needed to investigate the stress evolution in c-Si during the sequencial lithiation. Based on the classical diffusion equation (6) , the two-phase diffusion model is easily developed.

$$\frac{\partial c}{\partial t} = \nabla\cdot(D\nabla c) \quad (6)$$

where c is the normalized Li concentration (c = 0 for pure Si and c = 1 for $Li_{3.75}Si$) and D is the Li diffusivity. The sharp phase boundary is represented by a nonlinear diffusion coefficient as function of Li contents[60].

$$D = D_0\left[\frac{1}{1-c} - 2\alpha c\right] \quad (7)$$

where D_0 is the chemical diffusion coefficient and α is a constant to determine the thickness of phase boundary. The parameters are assigned as $\alpha = 1.95$ and $D_0 = 2.04\times 10^{-13}(\mathrm{cm}^2/\mathrm{s})$. We set $D_0 = 10^{-10}(\mathrm{cm}^2/\mathrm{s})$ in the twin defect.

Material Preparation

Preparation of the KIT-6 including polymer template: Pluronic P123 was dissolved in HCl solution and n-butanol was added and stirred at 35 °C for 1 hour to form a clear solution. After that, tetraethyl orthosilicate (12.9 g) was gently dropped into the above solution and kept at 35 °C for 24 hours under stirring. The mixture was then held at 120 °C for 24 hours for hydrothermal treatment. After washing in ethanol/HCl solution and drying, KIT-6 including the polymer template (KIT-6 w/ polymer template) was finally obtained. Also, the KIT-6 w/o polymer template was obtained through further calcination of the KIT-6 w/ polymer template at 600 °C for 2 hours under air atmosphere[35].

Preparation of the 3D-Si@SiO_x/C: the KIT-6 w/ polymer template (0.5 g) and magnesium powder (0.5 g, Sigma Aldrich, >99 %) were put separately inside an argon-filled and sealed stainless steel reactor (with inner volume of 3 cm^3), and then heated in a tube furnace at 750 °C for 2 hours under argon atmosphere with the ramping rate kept at 10 °C min^{-1}. The obtained black powder was first put into 1 M HCl (100 ml) for 12 hours under stirring, then washed with a mixed distilled water/ethanol solution by centrifugation for 5 times, and finally filtered and dried in a vacuum oven at 100 °C for 12 hours. By this process, magnesium oxide and magnesium silicide were removed, and the 3D-Si@SiO_x/C was obtained.

Structural Characterizations

Morphological observations and structural investigations of the prepared samples were conducted using a field emission scanning electron microscopy (FESEM, JEOL JSM-7000F) and transmission electron microscopy (TEM, JEOL JEM-2100F) equipped with electron energy loss spectroscopy (EELS). The X-ray diffraction patterns were collected using an X-ray diffractometer (Empyrean-XRD, PANalytical) with Cu Kα radiation (λ = 1.54056 Å). Raman spectra were obtained using a micro-Raman spectrometer (Bruker, Senterra) with a 532 nm laser. Thermogravimetric analysis (TGA) for determining the carbon content of of prepared samples was conducted using a TGA instrument (TG/DTA 6300, Perkin-Elmer) under air atmosphere. Specific surface areas and average pore diameters of the prepared samples were measured using a surface area and pore size analyzer (Tristar II 3020, Micromeritics) and calculated using the Brunauer-Emmett-Teller (BET) and Barrett-Joyner-Halenda (BJH) methods. To determine the surface and in-depth chemistry of the 3D-Si@SiO_x/C, X-ray photoelectron spectroscopy (XPS) measurements were performed using a surface analysis instrument (Sigma probe, Thermo Scientific) equipped with an argon ion beam sputtering system. In XPS measurements, XPS signals were continuously collected for a total of 21 times for 120 seconds with 6 second intervals of sputtering. The thermal stability of the 3D-Si@SiO_x/C and 3D-Si@SiO_x anodes were investigated using differential scanning calorimetry (DSC) measurements (STARe system, Mettler Toledo) at the state of full lithiation with the electrolyte.

Electrochemical Measurements

Working electrodes were prepared by coating a slurry containing 80 wt% active materials, 10 wt% polyacrylic acid (PAA) binder, and 10 wt% Super-P carbon conductor onto Cu foil

10 μm in thickness. After drying the electrodes in a convection oven at 80 °C for 6 hours and further drying in a vacuum oven at 120 °C for 12 hours, the electrodes were pressed to obtain the pre-set electrode density of 0.4 g cc^{-1}. The loading level of each electrode was fixed at 3.0 mg cm^{-2} for electrochemical measurements and 1.0 mg cm^{-2} for microscopy observations. CR2032 coin-type cells were assembled in an argon-filled glove box. In the coin cells, lithium metal foil and polyethylene membrane were used as the counter electrode and separator, respectively. 1 M $LiPF_6$ dissolved in mixed ethylene carbonate (EC) and ethyl methyl carbonate (EMC) with a volume ratio of 1:2, including 2 wt % of the additive fluoroethylene carbonate (FEC), was used as the electrolyte. The electrochemical tests were performed using a WBCS3000 (WonATech) workstation, and the cells were galvanostatically charged/discharged at various current densities within the voltage range of 0.01 V to 2.0 V *vs.* Li/Li^+. The electrochemical performance of the 3D-Si@SiO_x/C anode was also measured at high temperature (60 °C) to examine its thermal stability.

Density Functional Theory (DFT) calculations

Ab initio calculations for c-Si and twin boundary were performed using the DFT method with the generalized gradient approximation developed by Perdew, Burke and Ernzerhof (GGA-PBE). The projector augmented wave (PAW) method with a plane-wave basis set is employed using the Vienna Ab-initio Simulation Package (VASP)[61,62]. To describe the electron configurations for Si and Li, the valence subshells were set as $3s^2 3p^2$ for Si and $1s^2 2s^1$ for Li. With an energy cut-off of 500 eV, atomic structures, system energies, and mechanical stresses were calculated. A k-point mesh in the reciprocal-space was set to 5 × 5 × 5 for bulk Si and 5 × 5 × 1 for Si twin boundary using the Monkhorst–Pack scheme. Both the atomic positions and the supercell shape of c-Si were fully relaxed until the residual forces on each reached below 0.04 eV $Å^{-1}$. The lattice parameters of Si twin boundary were fixed at the initial values and then released in [111] direction only to ensure structural stability. To valid the Li diffusion behavior in the c-Si environment, Li migration pathways and activation energy barriers were calculated by the nudged elastic band (NEB) method.

Conflicts of interest

There are no conflicts to declare.

Author contributions

J.L. and J.H.K. conceived and designed the project. J.L. prepared the samples and performed the material characterizations, electrochemical measurements, and the corresponding data interpretations. J.M. carried out the computational simulations, calculations, and the corresponding data interpretations. S.A H. and J.K. assisted in the experiments. V.M. and Y.Y. assisted in and gave advice about the material preparation. Y.-U.H. carried out the TEM measurements and the data interpretations. H.K., Y.Y., and M.-S.P. supported the utilization of experimental facilities. H.K., S.-M.L., H.L., S.X.D., Y.Y., M.-S.P., and J.H.K. advised about the data analysis. J.L., J.M., and J.H.K. wrote the paper. J.H.K. and M.-S.P. organized the whole project.

Acknowledgements

This research was supported by the Technology Development Program to Solve Climate Changes through the National Research Foundation of Korea (NRF) funded by the Ministry of Science and Information and Communications Technology (ICT) (NRF-2018M1A2A2063347) and also supported by the Samsung Research Funding Center of Samsung Electronics (No. SRFC-TA1603-02).

References

1 C.-M. Park, J.-H. Kim, H. Kim and H.-J. Sohn, *Chemical Society Reviews*, 2010, **39**, 3115-3141.
2 M. Armand and J. M. Tarascon, *Nature*, 2008, **451**, 652.
3 C. K. Chan, H. Peng, G. Liu, K. Mcllwrath, X. F. Zhang, R. A. Huggins and Y. Cui, *Nature Nanotechnology*, 2007, **3**, 31.
4 W. Kohs, H. J. Santner, F. Hofer, H. Schröttner, J. Doninger, I. Barsukov, H. Buqa, J. H. Albering, K. C. Möller, J. O. Besenhard and M. Winter, *Journal of Power Sources*, 2003, **119-121**, 528-537.
5 X. Zuo, J. Zhu, P. Müller-Buschbaum and Y.-J. Cheng, *Nano Energy*, 2017, **31**, 113-143.
6 U. Kasavajjula, C. Wang and A. J. Appleby, *Journal of Power Sources*, 2007, **163**, 1003-1039.
7 W.-J. Zhang, *Journal of Power Sources*, 2011, **196**, 13-24.
8 N. Liu, H. Wu, M. T. McDowell, Y. Yao, C. Wang and Y. Cui, *Nano Letters*, 2012, **12**, 3315-3321.
9 L. Y. Yang, H. Z. Li, J. Liu, Z. Q. Sun, S. S. Tang and M. Lei, *Scientific Reports*, 2015, **5**, 10908.
10 G. Liang, X. Qin, J. Zou, L. Luo, Y. Wang, M. Wu, H. Zhu, G. Chen, F. Kang and B. Li, *Carbon*, 2018, **127**, 424-431.
11 A. M. Chockla, K. C. Klavetter, C. B. Mullins and B. A. Korgel, *Chemistry of Materials*, 2012, **24**, 3738-3745.
12 A. Gohier, B. Laïk, J.-P. Pereira-Ramos, C. S. Cojocaru and P. Tran-Van, *Journal of Power Sources*, 2012, **203**, 135-139.
13 Z. Wen, G. Lu, S. Mao, H. Kim, S. Cui, K. Yu, X. Huang, P. T. Hurley, O. Mao and J. Chen, *Electrochemistry Communications*, 2013, **29**, 67-70.
14 X. Wang, L. Sun, X. Hu, R. A. Susantyoko and Q. Zhang, *Journal of Power Sources*, 2015, **280**, 393-396.
15 X. Yu, F. Xue, H. Huang, C. Liu, J. Yu, Y. Sun, X. Dong, G. Cao and Y. Jung, *Nanoscale*, 2014, **6**, 6860-6865.
16 Y. Liu, B. Chen, F. Cao, H. L. W. Chan, X. Zhao and J. Yuan, *Journal of Materials Chemistry*, 2011, **21**, 17083-17086.
17 Z. Jiang, C. Li, S. Hao, K. Zhu and P. Zhang, *Electrochimica Acta*, 2014, **115**, 393-398.
18 Q. Xiao, M. Gu, H. Yang, B. Li, C. Zhang, Y. Liu, F. Liu, F. Dai, L. Yang, Z. Liu, X. Xiao, G. Liu, P. Zhao, S. Zhang, C. Wang, Y. Lu and M. Cai, *Nature Communications*, 2015, **6**, 8844.
19 J.-I. Lee, K. T. Lee, J. Cho, J. Kim, N.-S. Choi and S. Park, *Angewandte Chemie International Edition*, 2012, **51**, 2767-2771.
20 Y. Li, K. Yan, H.-W. Lee, Z. Lu, N. Liu and Y. Cui, *Nature Energy*, 2016, **1**, 15029.
21 S. Choi, T.-w. Kwon, A. Coskun and J. W. Choi, *Science*, 2017, **357**, 279.

22 R. Zhang, Y. Du, D. Li, D. Shen, J. Yang, Z. Guo, H. K. Liu, A. A. Elzatahry and D. Zhao, *Advanced Materials*, 2014, **26**, 6749-6755.
23 A. Magasinski, P. Dixon, B. Hertzberg, A. Kvit, J. Ayala and G. Yushin, *Nature Materials*, 2010, **9**, 353.
24 M. Ko, S. Chae, S. Jeong, P. Oh and J. Cho, *ACS Nano*, 2014, **8**, 8591-8599.
25 J.-K. Yoo, J. Kim, Y. S. Jung and K. Kang, *Advanced Materials*, 2012, **24**, 5452-5456.
26 H. Wu, G. Chan, J. W. Choi, I. Ryu, Y. Yao, M. T. McDowell, S. W. Lee, A. Jackson, Y. Yang, L. Hu and Y. Cui, *Nature Nanotechnology*, 2012, **7**, 310.
27 E. Park, H. Yoo, J. Lee, M.-S. Park, Y.-J. Kim and H. Kim, *ACS Nano*, 2015, **9**, 7690-7696.
28 R. Ma, Y. Liu, Y. Yang, M. Gao and H. Pan, *Applied Physics Letters*, 2014, **105**, 213901.
29 H. Jung, Y.-U. Kim, M.-S. Sung, Y. Hwa, G. Jeong, G.-B. Kim and H.-J. Sohn, *Journal of Materials Chemistry*, 2011, **21**, 11213-11216.
30 R. Dash and S. Pannala, *Scientific Reports*, 2016, **6**, 27449.
31 M. Yoshio, H. Wang, K. Fukuda, T. Umeno, N. Dimov and Z. Ogumi, *Journal of The Electrochemical Society*, 2002, **149**, A1598-A1603.
32 Z. Bao, M. R. Weatherspoon, S. Shian, Y. Cai, P. D. Graham, S. M. Allan, G. Ahmad, M. B. Dickerson, B. C. Church, Z. Kang, H. W. Abernathy Iii, C. J. Summers, M. Liu and K. H. Sandhage, *Nature*, 2007, **446**, 172.
33 K. P. Gierszal, T.-W. Kim, R. Ryoo and M. Jaroniec, *The Journal of Physical Chemistry B*, 2005, **109**, 23263-23268.
34 J. H. Moon, Y. Xu, Y. Dan, S. M. Yang, A. T. Johnson and S. Yang, *Advanced Materials*, 2007, **19**, 1510-1514.
35 Y. Doi, A. Takai, Y. Sakamoto, O. Terasaki, Y. Yamauchi and K. Kuroda, *Chemical Communications*, 2010, **46**, 6365-6367.
36 A. M. Morales and C. M. Lieber, *Science*, 1998, **279**, 208.
37 M.-S. Park, E. Park, J. Lee, G. Jeong, K. J. Kim, J. H. Kim, Y.-J. Kim and H. Kim, *ACS Applied Materials & Interfaces*, 2014, **6**, 9608-9613.
38 K. Ariga, A. Vinu, Y. Yamauchi, Q. Ji and J. P. Hill, *Bulletin of the Chemical Society of Japan*, 2011, **85**, 1-32.
39 P. Gao, H. Tang, A. Xing and Z. Bao, *Electrochimica Acta*, 2017, **228**, 545-552.
40 J. Entwistle, A. Rennie and S. Patwardhan, *Journal of Materials Chemistry A*, 2018, DOI: 10.1039/C8TA06370B.
41 W. Chen, Z. Fan, A. Dhanabalan, C. Chen and C. Wang, *Journal of The Electrochemical Society*, 2011, **158**, A1055-A1059.
42 E. Park, M.-S. Park, J. Lee, K. J. Kim, G. Jeong, J. H. Kim, Y.-J. Kim and H. Kim, *ChemSusChem*, 2015, **8**, 688-694.
43 A. Janotta, Y. Dikce, M. Schmidt, C. Eisele, M. Stutzmann, M. Luysberg and L. Houben, *Journal of Applied Physics*, 2004, **95**, 4060-4068.
44 A. C. Ferrari, *Solid State Communications*, 2007, **143**, 47-57.
45 M. Miyachi, H. Yamamoto, H. Kawai, T. Ohta and M. Shirakata, *Journal of The Electrochemical Society*, 2005, **152**, A2089-A2091.
46 S. T. Jackson and R. G. Nuzzo, *Applied Surface Science*, 1995, **90**, 195-203.
47 R. C. Newman, *Reports on Progress in Physics*, 1982, **45**, 1163.
48 C.-Y. Wang, L.-J. Yang, W. Zhao, Q.-Y. Meng, G.-X. Wu, B.-L. Wang and C.-L. Li, *Journal of Applied Physics*, 2014, **116**, 213504.
49 J. Wang, X. Meng, X. Fan, W. Zhang, H. Zhang and C. Wang, *ACS Nano*, 2015, **9**, 6576-6586.
50 N. Liu, Z. Lu, J. Zhao, M. T. McDowell, H.-W. Lee, W. Zhao and Y. Cui, *Nature Nanotechnology*, 2014, **9**, 187.
51 H. Kim, K. E. Kweon, C.-Y. Chou, J. G. Ekerdt and G. S. Hwang, *The Journal of Physical Chemistry C*, 2010, **114**, 17942-17946.
52 J. Moon, B. Lee, M. Cho and K. Cho, *Journal of Power Sources*, 2014, **272**, 1010-1017.
53 J. W. Wang, Y. He, F. Fan, X. H. Liu, S. Xia, Y. Liu, C. T. Harris, H. Li, J. Y. Huang, S. X. Mao and T. Zhu, *Nano Letters*, 2013, **13**, 709-715.
54 M. Winter and R. J. Brodd, *Chemical Reviews*, 2004, **104**, 4245-4270.
55 I. A. Profatilova, C. Stock, A. Schmitz, S. Passerini and M. Winter, *Journal of Power Sources*, 2013, **222**, 140-149.
56 G. Jeong, J.-G. Kim, M.-S. Park, M. Seo, S. M. Hwang, Y.-U. Kim, Y.-J. Kim, J. H. Kim and S. X. Dou, *ACS Nano*, 2014, **8**, 2977-2985.
57 J. Cho, *Journal of Materials Chemistry*, 2010, **20**, 4009-4014.
58 Y. Shi, J. Zhang, L. Pan, Y. Shi and G. Yu, *Nano Today*, 2016, **11**, 738-762.
59 V. B. Shenoy, P. Johari and Y. Qi, *Journal of Power Sources*, 2010, **195**, 6825-6830.
60 H. Yang, F. Fan, W. Liang, X. Guo, T. Zhu and S. Zhang, *Journal of the Mechanics and Physics of Solids*, 2014, **70**, 349-361.
61 P. E. Blöchl, *Physical Review B*, 1994, **50**, 17953-17979.
62 G. Kresse and J. Hafner, *Physical Review B*, 1993, **48**, 13115-13118.

Electronic Supplementary Information

Everlasting Living and Breathing Gyroid 3D Network in Si@SiO_x/C Nanoarchitecture for Paving the Way to High Energy Lithium Storage Materials

Jaewoo Lee‡[a], Janghyuk Moon‡[b], Sang A Han[a,c], Junyoung Kim[d], Victor Malgras[e], Yoon-Uk Heo[f], Hansu Kim[g], Sang-Min Lee[h], Huakun Liu[a], Shi Xue Dou[a], Yusuke Yamauchi[i], Min-Sik Park*[d] and Jung Ho Kim*[a]

a. Institute for Superconducting & Electronic Materials (ISEM), Australian Institute of Innovative Materials (AIIM), University of Wollongong, Innovation Campus, Squires Way, North Wollongong, NSW 2500, Australia, E-mail: jhk@uow.edu.au

b. School of Energy Systems Engineering, Chung-Ang University, Seoul, Republic of Korea

c. School of Advanced Materials Science & Engineering, Sungkyunkwan University (SKKU), Suwon, 440-746, Republic of Korea

d. Department of Advanced Materials Engineering for Information and Electronics, Kyung Hee University, 1732 Deogyeong-daero, Giheung-gu, Yongin 17104, Republic of Korea, E-mail: mspark@khu.ac.kr

e. International Center for Young Scientists (ICYS) & International Centre for Materials Nanoarchitectonics (MANA), National Institute for Materials Science (NIMS), 1-1 Namiki, Tsukuba, Ibaraki 305-0044, Japan

f. Graduate Institute of Ferrous Technology (GIFT), Pohang University of Science and Technology (POSTECH), San 31, Hyoja-Dong, Pohang 790-784, Republic of Korea

g. Department of Energy Engineering, Hanyang University, 222 Wangsimni-ro, Seongdong-gu, Seoul, 133–791, Republic of Korea

h. Battery Research Center, Korea Electrotechnology Research Institute, 12 Bulmosan-ro, 10 beon-gil, Seongsan-gu, Changwon 51543, Republic of Korea

i. School of Chemical Engineering and Australian Institute for Bioengineering and Nanotechnology (AIBN), The University of Queensland, Brisbane, QLD 4072, Australia

‡ These authors contributed equally to this work.

Gyroid structure

$$\sin x * \cos y + \sin y * \cos z + \sin z * \cos x = t$$

$$0 \leq |t| \leq \sqrt{2}$$

Double gyroid structure

$$\sin x * \cos y + \sin y * \cos z + \sin z * \cos x = \pm t$$

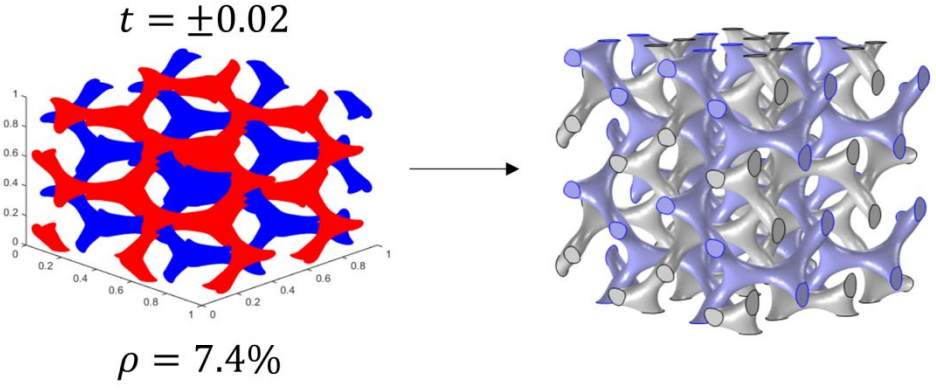

Fig. S1 Gyroid and double-gyroid structure modeling for the continuum scale analysis.

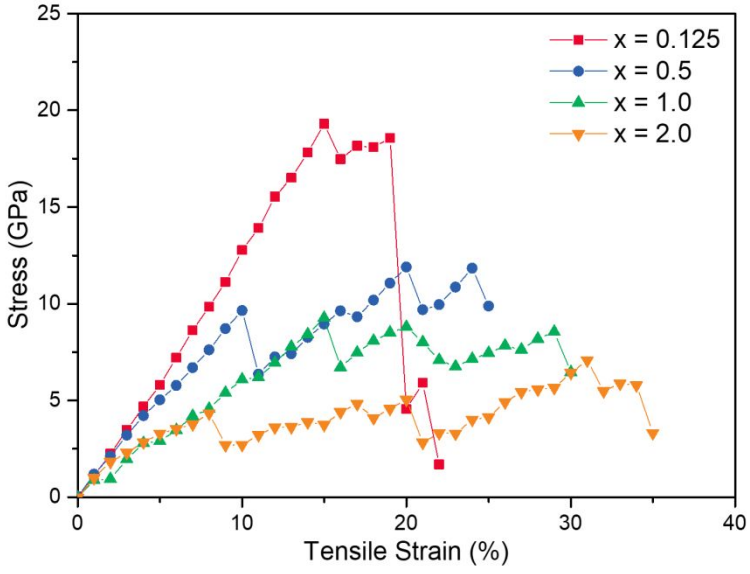

Fig. S2 Stress and strain curves of lithiated amorphous SiO_2 (Li_xSiO_2, x = 0.0125, 0.5, 1.0, and 2.0) based on first-principles calculations.

The amorphous structures containing 32 Si and 64 O atoms with periodic boundary conditions were generated by rapid melting-quenching ab-initio molecular dynamics simulation at high temperature. A supercell with this atomic number is consciously relatively small. Our choice of supercell, however, affords such studies at a reasonable balance of computational cost and accuracy. These model structures can explore a large number of possible configurations of Si structures with various Li contents with good statistical accuracy.

The stress-strain response curves of four representative Li_xSiO_2 compositions (where x represents the atomic ratio of Li in SiO_2) are shown in Fig. S2. The uniaxial tension of Li_xSiO_2 is simulated by applying a constant strain and full atomic relaxation. To consider Poisson's effect, the constraint of in-plane direction of the unit-cell is removed.

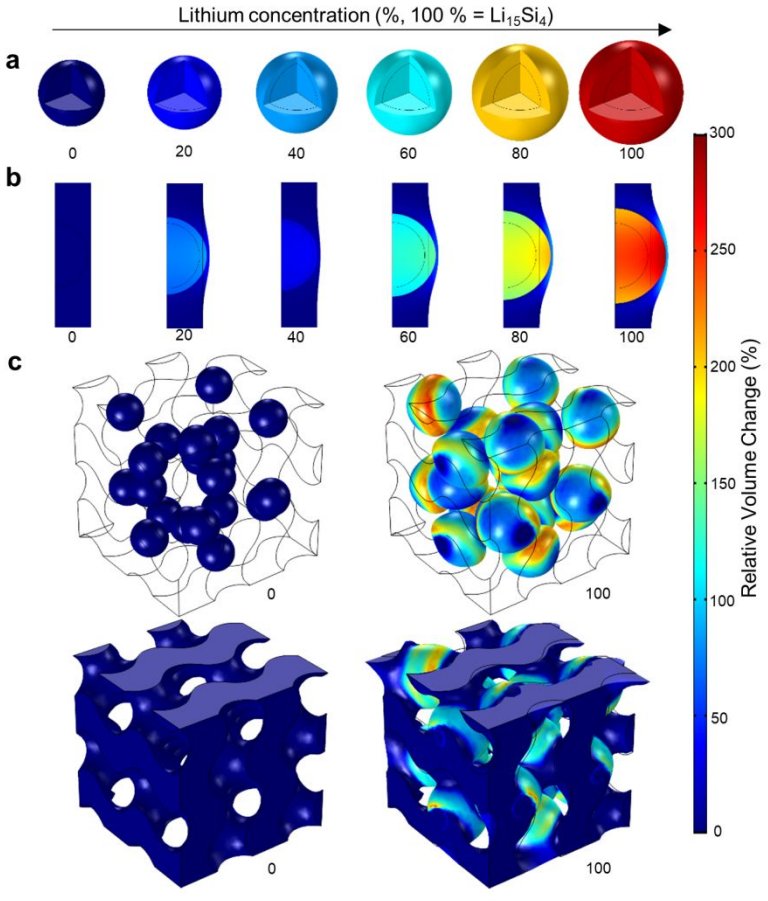

Fig. S3 Continuum scale analysis for the simulation of particle and unit volume changes in silicon-based materials before and after full lithiation. (a) Si nanoparticle in free space, (b) Si nanoparticle embedded in 1D SiO_x structure, (c) Si nanoparticles embedded in gyroid 3D network structure and the total unit of the gyroid 3D network for Si@SiO_x.

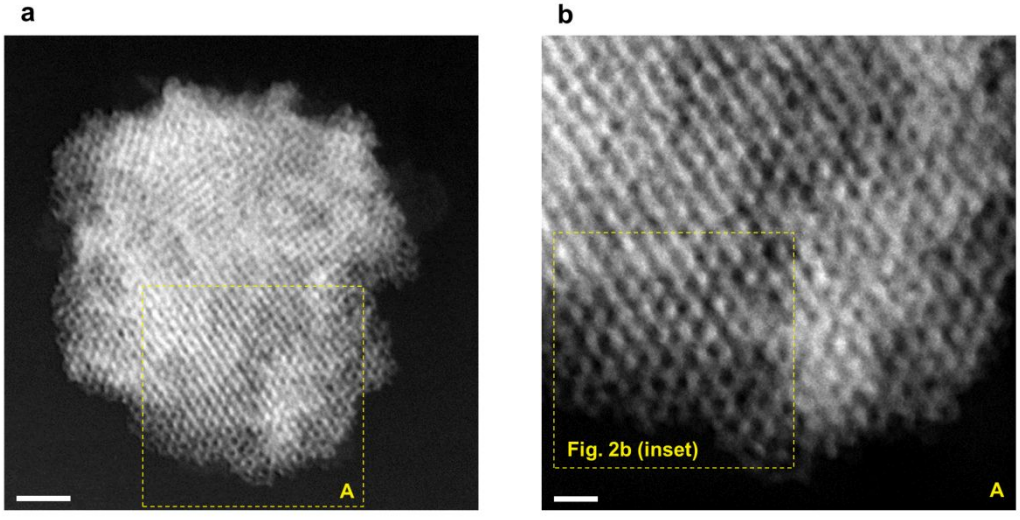

Fig. S4 HAADF-STEM images of highly ordered double-gyroid KIT-6 including a polymer template. Scale bars, 50 nm for (a), 20 nm for (b)

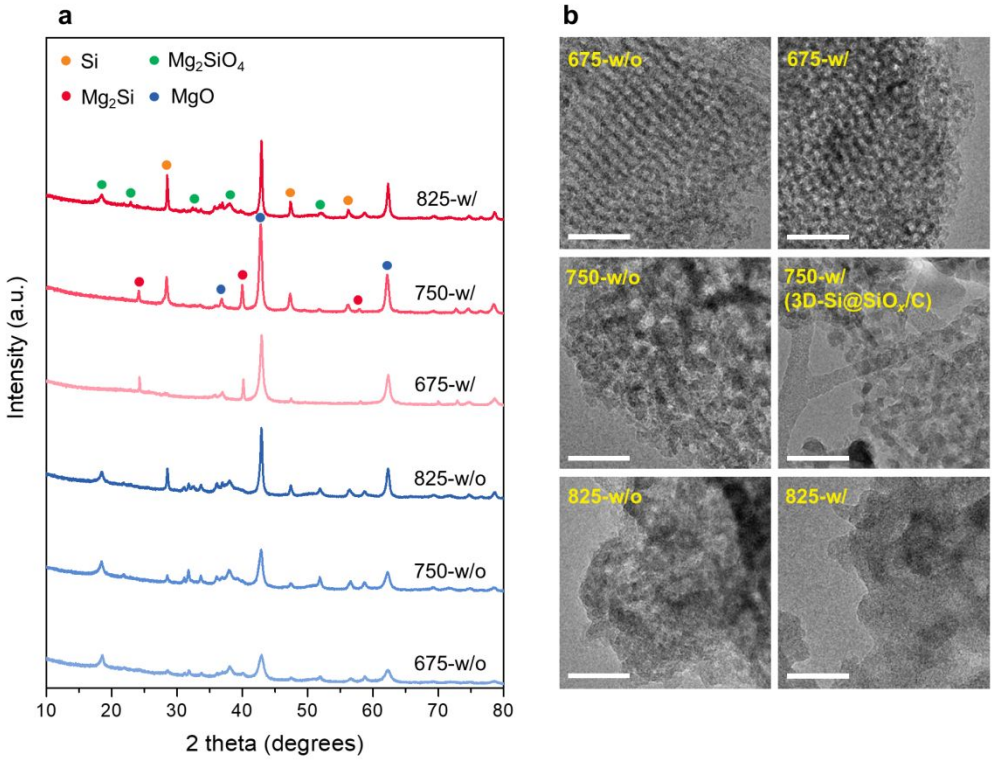

Fig. S5 (a) XRD patterns collected before HCl washing, (b) TEM images of samples obtained under different synthesis conditions. (w/ / w/o: synthesized from calcined / uncalcined KIT-6, 675 / 750 / 825: synthesis temperatures) Scale bars, 50 nm for (b)

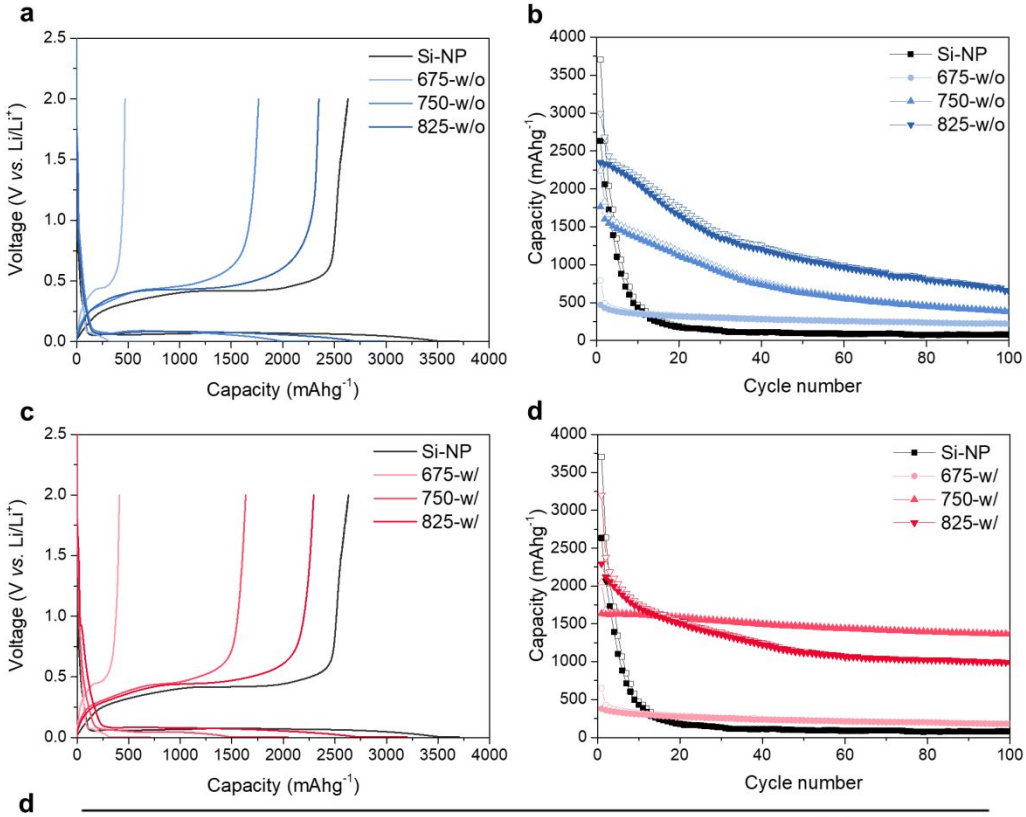

d

	Si-NP	675-w/o	750-w/o	825-w/o	675-w/	750-w/	825-w/
Charge Capacity (mAh/g)	3704	793	2235	2990	706	2043	3196
Discharge Capacity (mAh/g)	2631	471	1765	2349	410	1635	2294
ICE (%)	71.1	59.4	79.0	78.6	58.0	80.1	71.8
Capacity Retention (%)	3.0	46.8	21.7	24.8	47.3	83.3	43.1

Fig. S6 Galvanostatic charge-discharge profiles (a, c) and cycling performances (b, d) of three w/o samples (a, b) and three w/ samples (c, d) with Si-NP anode. (e) Table of their electrochemical properties. (w/ / w/o: synthesized from calcined / uncalcined KIT-6, 675 / 750 / 825: synthesis temperatures, ICE: initial Coulombic efficiency)

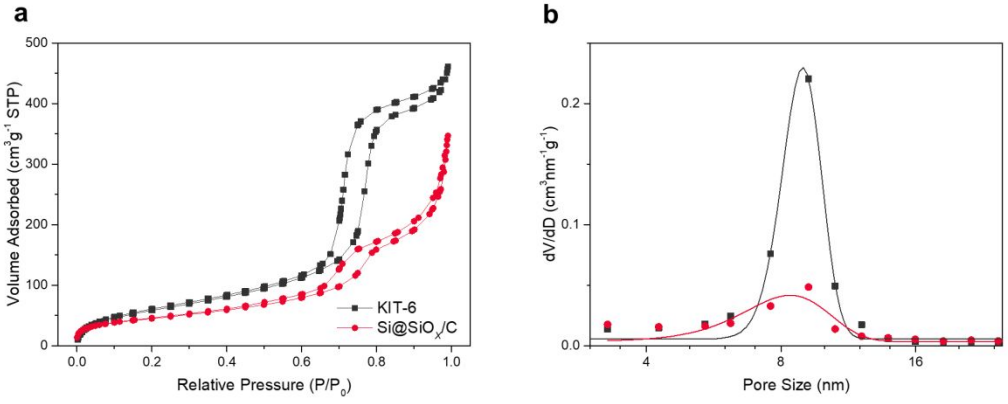

c

Samples	Surface Area (m^2/g)	Average Pore Diameter (nm)
KIT-6	225	8.9
3D-Si@SiO$_x$/C	161	8.7

Fig. S7 (a) N_2 adsorption/desorption isotherms and (b) pore size distributions of the KIT-6 including the polymer template and the 3D-Si@SiO$_x$/C. (c) Table of calculated surface area and average pore diameter, as determined by the Brunauer-Emmett-Teller (BET) and Barrett-Joyner-Halenda (BJH) methods, respectively.

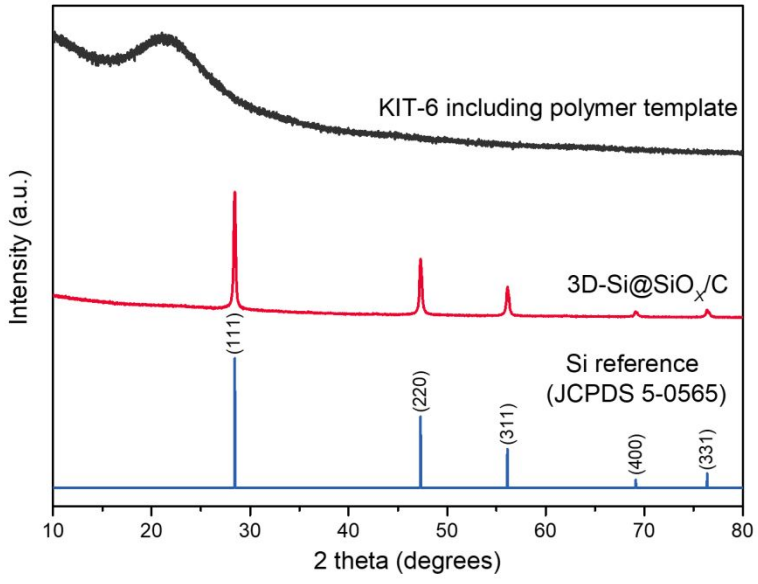

Fig. S8 XRD patterns of the KIT-6 including the polymer template (precursor) and the 3D-Si@SiO_x/C (product).

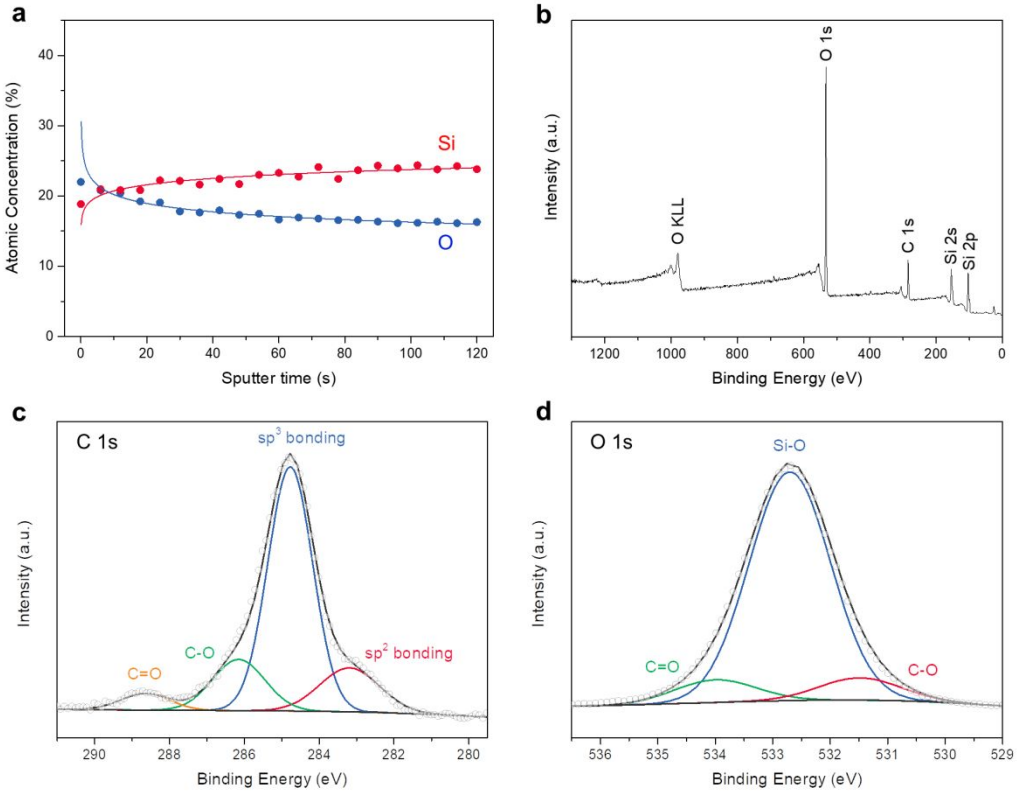

Fig. S9 (a) XPS depth profiling, and (b) survey, (c) C 1s, and (d) O 1s spectra of the 3D-Si@SiO_x/C.

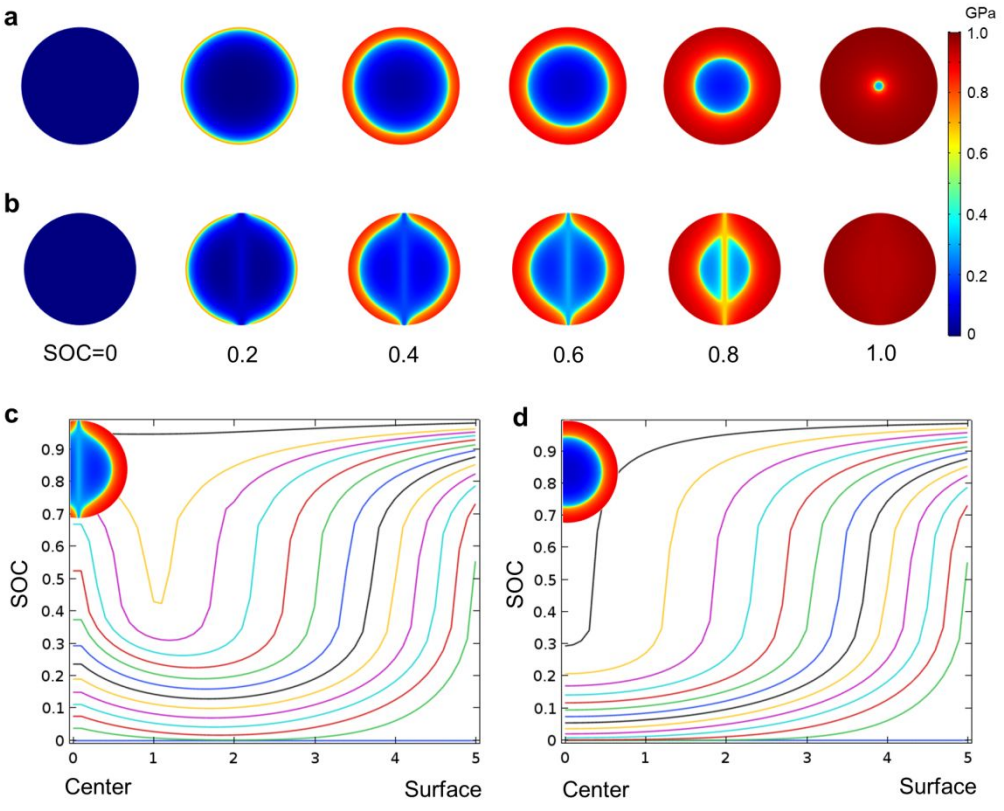

Fig. S10 Continuum scale analysis for the lithiation evolution of a crystalline Si particle. Li contour plots during Li evolution (a) without and (b) with a twin defect. Normalized radial Li concentration distribution during lithiation (c) with and (d) without a twin defect. (SOC: state of charge)

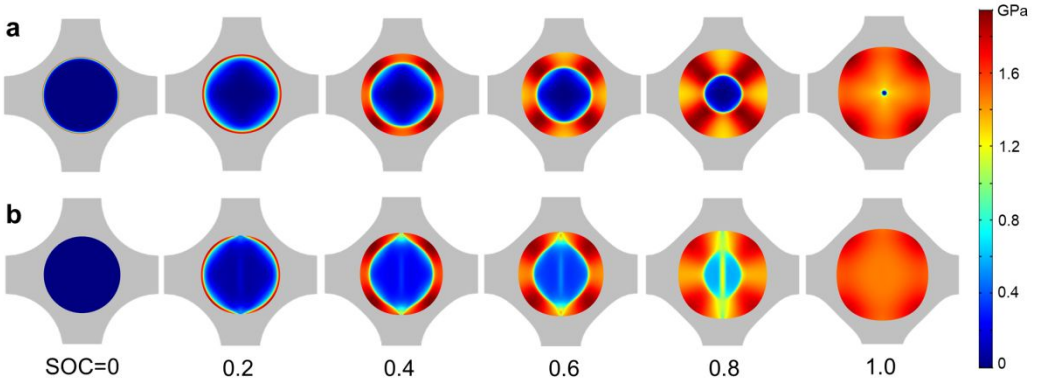

Fig. S11 The von Mises stress evolution of a crystalline Si particle in the gyroid structure (a) without and (b) with a twin defect during lithiation. (SOC: state of charge)

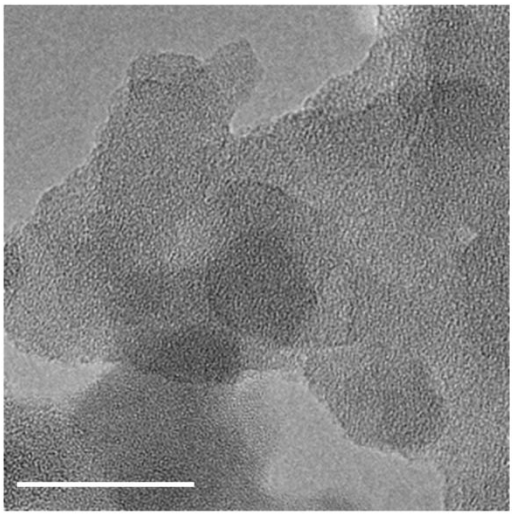

Fig. S12 HRTEM observation of partially collapsed 3D-Si@SiO_x/C particles after 100 cycles. Scale bar, 20 nm

Description of Additional Supplementary Files

1. File name: Movie 1
   Description: volume changes of the Si NP in free space (fig. 1a) while the Si particle occurs gradual lithiation up to $Li_{3.75}Si$

2. File name: Movie 2
   Description: volume changes of the Si NP in 1D-SiO_x (fig. 1b) while the Si particle occurs gradual lithiation up to $Li_{3.75}Si$

3. File name: Movie 3
   Description: volume changes of the Si NPs in gyroid 3D network SiO_x (fig. 1c, up) while the Si particles occur gradual lithiation up to $Li_{3.75}Si$

4. File name: Movie 4
   Description: volume changes of the total unit of gyroid 3D network Si@SiO_x (fig. 1c, down) while the Si particles occur gradual lithiation up to $Li_{3.75}Si$